17

Water Sorption Applications of MOFs

17.1 Introduction

The use of metal-organic frameworks (MOFs) in water sorption-based applications has attracted much interest. Such applications include adsorption-driven heat pumps (ADHPs), seawater desalination, drying of gas streams, humidity control in buildings, and water harvesting from air. All of these applications pose different requirements to the adsorbent in terms of its adsorption behavior [1]. The modular structure of MOFs makes them ideal candidates for such applications because it enables chemists to design their sorption properties with respect to parameters such as the total uptake, the position of the uptake on the P/P_0 scale, and the adsorption mechanism.

Even though all examples for processes involving the adsorption of water described above are fundamentally different and require significantly different adsorption properties, they all require the MOF adsorbent to be hydrolytically stable, have a high adsorption capacity, and have a high selectivity for water. This chapter will cover the principles of water vapor sorption in MOFs, provide guidelines for the design of next generation MOFs, and illustrate ways to optimize the water sorption properties of a given material. The adsorption of other vapors in MOFs have the same underlying general principles and are not discussed here.

17.2 Hydrolytic Stability of MOFs

Many MOFs, especially first-generation materials, undergo structural degradation in the presence of water. With respect to hydrolytic stability, we distinguish thermodynamic and kinetic factors (Table 17.1). It is important to note that with respect to thermodynamics the terms stable and unstable are used, while in the context of kinetics the corresponding terms are inert and labile. The fact that the hydrolytic stability of MOFs is related to specific structural allows to delineate strategies for the design of hydrolytically stable MOFs. In the following sections we will discuss the degradation of MOFs in the presence of water and derive principles for the design of hydrolytically stable MOFs.

Introduction to Reticular Chemistry: Metal-Organic Frameworks and Covalent Organic Frameworks,
First Edition. Omar M. Yaghi, Markus J. Kalmutzki, and Christian S. Diercks.

Companion website: www.wiley.com/go/yaghi/reticular

Table 17.1 Structural factors influencing the thermodynamic and kinetic stability of MOFs in the presence of water.

Thermodynamic stability/instability	Kinetic inertness/lability
• pK_a of the linker (basicity) • Oxidation state and ionic radius of the metal (acidity) • Reduction potential of the metal • Coordination geometry	• Steric hindrance (i.e. "coordination number") and rigidity of the constituents • Steric hindrance through interpenetration • Hydrophobicity • Electronic configuration of the metal ions

17.2.1 Experimental Assessment of the Hydrolytic Stability

The hydrolytic stability of MOFs is typically determined by comparing powder X-ray diffraction (PXRD) patterns before and after exposure to a specific amount of water (e.g. atmosphere with defined relative humidity, RH). While partial collapse of the pores only results in broadening of the reflection peaks due to partial loss of crystallinity and the formation of an amorphous side phase, the decomposition of MOFs by hydrolysis typically leads to complete amorphization and consequently the disappearance of all reflections in the PXRD pattern. To substantiate information gained from X-ray diffraction experiments it is instructive to compare surface areas calculated from gas adsorption measurements prior to and after exposure to humidity. Another decomposition pathway is the partial dissolution of MOFs. This inevitably leads to a mass loss, which is verified by weighing the MOF before and after it has been exposed to water.

To study the effects of water vapor on MOFs for specific applications, the gas composition should resemble that under application condition, e.g. $H_2O/CO_2/N_2$ 1 : 1.5 : 7.5 for carbon capture from post-combustion flue gas. In contrast, the isolated effect of water vapor on a MOF structure is studied using inert carrier gases such as N_2, He, and Ar and true water vapor adsorption isotherms can only be acquired when water vapor is dosed into the material in the absence of carrier gases.

Different applications require specific levels of hydrolytic stability. Minimum testing conditions for MOFs in "single-pass" and "cycled" applications, as well as liquid phase separation have been established and an overview is given in Table 17.2. While the abovementioned methods give information about the hydrolytic stability of MOFs, they provide little to no insight into the mechanism of degradation.

17.2.2 Degradation Mechanisms

The degradation of MOFs in the presence of water can occur either by hydrolysis or by linker replacement [2]. Hydrolysis is initiated by the cleavage of the metal–linker bond. Subsequently, a hydroxylated secondary building unit (SBU) is formed and the linker is released in its protonated (neutral) form.

$$M^{n+} - {}^{-}(O_2C)\text{-}R + H_2O \longrightarrow M^{n+} - (OH)^{-} + R\text{-}(CO_2H)$$

Table 17.2 Testing conditions to determine the water stability of a given material for different types of application.

Application	Testing conditions	Characterization methods
Gas or vapor phase		
Single pass/one-time use		
Single pass cartridge (e.g. gas mask or air filters)	Prolonged stability in ambient or humidified air	PXRD and sorption (BET)[a] measurements
Cycled/multiple use		
Gas separation packed bed (e.g. CO_2, NG, H_2)	Multiple adsorption desorption cycles with the relevant gas mixture (regeneration with the appropriate method; TSA[b], PSA[c], VSA[d])	PXRD, sorption (BET) measurements, adsorption capacity for each cycle, microscopy (e.g. SEM[e], TEM[f])
Gas separation membranes	Prolonged exposure to the relevant gas mixture under application conditions	PXRD, sorption (BET) measurements, microscopy (e.g. SEM, TEM, AFM[g])
Gas storage (e.g. H_2, CH_4, CO_2)	Prolonged storage of the relevant gas under application pressures	PXRD and sorption (BET) measurements, microscopy (e.g. SEM, TEM)
Aqueous phase		
Liquid phase catalysis, capture of molecules from aq. solutions, liquid phase separation	Immersion and prolonged stirring under relevant application conditions	PXRD and sorption (BET) measurements, solid-state mass loss, titration of the solution

a) Brunauer–Emmett–Teller surface area.
b) Temperature swing adsorption.
c) Pressure swing adsorption.
d) Vacuum swing adsorption.
e) Scanning electron microscope.
f) Transmission electron microscope.
g) Atomic force microscope.

The mechanism of linker displacement can be described as the insertion of water into the metal–linker bond. This leads to the formation of a hydrated SBU and the release of a deprotonated linker.

$$M^{n+} - {}^{-}(O_2C)\text{-}R + H_2O \longrightarrow M^{n+} - (OH_2) + R\text{-}(CO_2)^{-}$$

Ligand displacement is the most likely mechanism for the structural degradation of UiO-66 in neutral or basic aqueous conditions, whereas in the presence of acids another mechanism prevails [3]. Figure 17.1 illustrates the degradation of UiO-66 in the presence of water, base, and acid. Treatment with water leads to the hydration of the SBU and release of a deprotonated linker following the hydrolysis mechanism (Figure 17.1a). A similar mechanism (solvolysis) is suggested for the treatment of UiO-66 with alcohols such as methanol. Basic hydrolysis

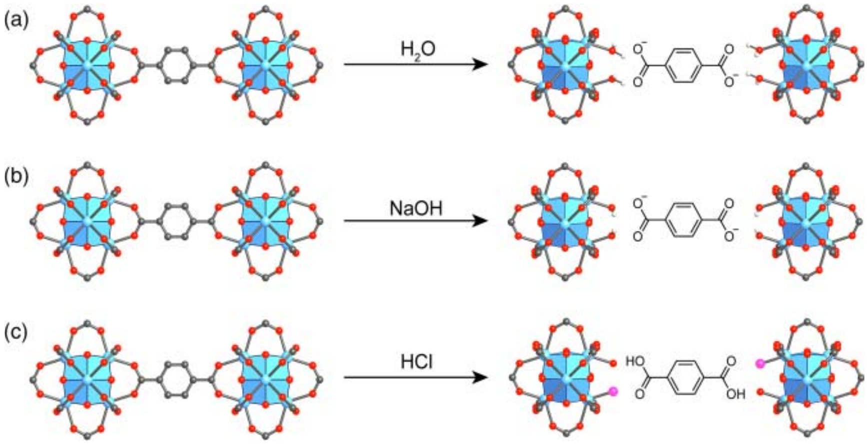

Figure 17.1 Degradation mechanisms of UiO-66 in the presence of water, base, and hydrochloric acid. (a) Hydrolysis in water affords the formation of a hydrated SBU, whereas (b) hydroxylation of the SBU affords the release of a deprotonated linker. (c) Treatment with HCl causes the chlorination of the SBU while the linker is released in its protonated neutral from. Color code: Zr, blue; C, gray; O, red; Cl, pink.

affords the hydroxylation of the SBU and the release of the deprotonated linker (Figure 17.1b), whereas acid treatment with hydrochloric acid gives the chlorinated SBU and the linker is released in its protonated form (Figure 17.1c). The chlorinated SBU may subsequently be hydrolyzed to give a neutral SBU bearing one addition –OH and one $-OH_2$ ligand.

17.2.3 Thermodynamic Stability

The thermodynamic stability is mainly defined by two factors: (i) the stability of the metal–linker bond and (ii) the energetic position of the frontier orbitals of the metal relative to those of water. It is easy to approximate the stability of the metal–linker bond, but it is more challenging to make a statement about the energetics of the frontier orbitals.

17.2.3.1 Strength of the Metal–Linker Bond

The covalent nature of the organic linkers renders them highly chemically stable entities and the molecular analogs of most SBUs are known to be stable in water. The weak point in the extended structure formed by their reticulation is the bond between them and its strength can (to some extent) be used as a measure of the hydrolytic stability of a MOF. The interaction between the metal centers in the SBU and the binding groups of the organic linker can be approximated as a Lewis acid–base interaction. This implies that the higher the pK_a of the protonated linker, the stronger the metal–linker bond as illustrated by the high hydrolytic stability of pyrazolate-based MOFs [4]. A comparison of di- and tritopic pyrazolate and carboxylate linkers based on a central aryl unit reveals dramatic differences in pK_a between these two binding groups (see Figure 17.2a). The higher pK_a values

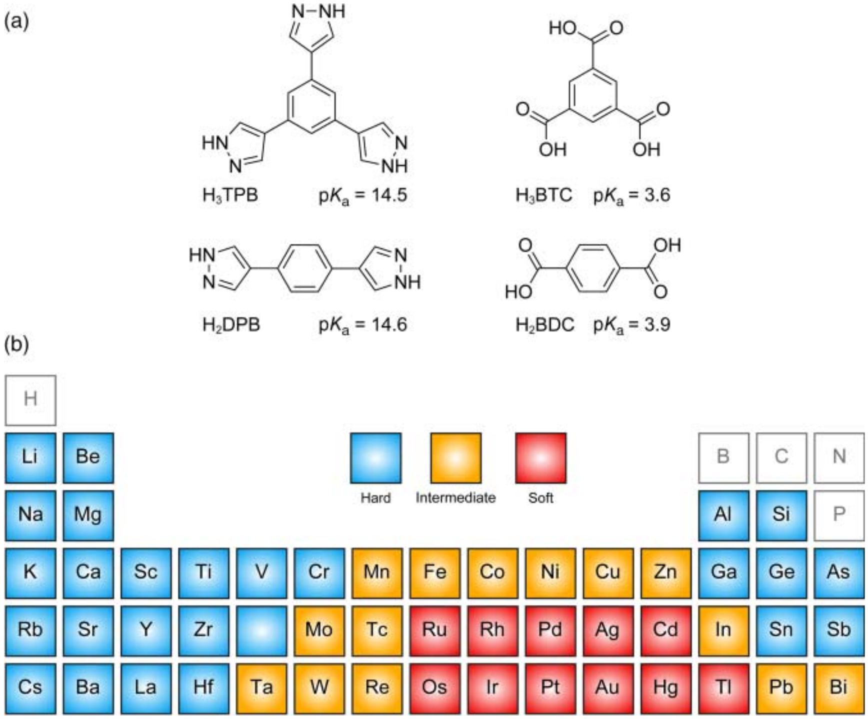

Figure 17.2 (a) Linker molecules with different binding groups and the corresponding pK_a values. Pyrazole is a weaker acid (the corresponding base is strong) and the resulting M—N bond is therefore thermodynamically more stable than the M—O bond in carboxylate-based MOFs. (b) Hard, intermediate, and soft acids and their position in the periodic table.

of the pyrazole-based linkers imply stronger bonding to the metal component of the framework and therefore a higher hydrolytic stability.

The chemical nature of the metal center determines the strength of the metal–linker bond in a similar way. The higher the charge on the metal and the smaller its radius, the more acidic it is, leading to stronger bonding with the organic linker. The radius and the precise electronic structure of the metal greatly influence the bond strength. This is best described by the hard–soft acid–base (HSAB) concept, which states that frontier orbitals of similar size and polarizability can overlap to form strong bonds. For MOFs, this means that the bond between hard carboxylate binding groups and hard Ti^{4+} centers (high charge/radius ratio) is stronger than that of hard carboxylate binding groups and soft Hg^{2+} centers (low charge/radius ratio). Figure 17.2b shows a periodic table where the metals have been divided into three categories: (i) hard acid, (ii) intermediate acid, and (iii) soft acid. The thermodynamic stability can correlate with the hydrolytic stability, but other factors must be taken into consideration as well.

17.2.3.2 Reactivity of Metals Toward Water

Considerations of the metal–linker bond strength based on pK_a values and the HSAB concept can serve as simple tools to approximate the stability of

MOFs. With respect to the hydrolytic stability, other thermodynamic factors such as the position of the metal frontier orbital with respect to those of water are important. The energetic position of the frontier orbitals of metal ions correlates with their reduction potential. The comparison of PXRD patterns of Co_2Cl_2(BTDD) (BTDD = (bis(1*H*-1,2,3-triazolo[4,5-*b*],[4′,5′-*i*])dibenzo[1,4] dioxin) and Mn_2Cl_2(BTDD) measured after exposure to moisture shows no changes for Co_2Cl_2(BTDD), whereas amorphization of Mn_2Cl_2(BTDD) is observed. When we consider the standard reduction potentials of Co^{2+} and Mn^{2+} we see that the reduction potential of Co^{2+} ($E^0 = -0.28\,V$) is less negative than that of Mn^{2+} ($E^0 = -1.18\,V$) [5]. As a rule of thumb, we can say that for a series of isoreticular MOFs constructed from different metals, those containing metals with lower (or more negative) reduction potentials are more likely to undergo hydrolysis [6].

17.2.4 Kinetic Inertness

A thermodynamically unstable MOF does not necessarily degrade in the presence of water. This is explained by the fact that thermodynamically unstable compounds can be kinetically inert, thus preventing their hydrolysis. Thermodynamic stability is related to the Gibbs free energy (ΔG) of the reaction, whereas kinetic inertness is related to the activation energy (E_a) of the reaction. Therefore, the products of hydrolysis may be of lower energy and thus represent the thermodynamically more stable state (ΔG more negative); however, the activation barrier may be too high to overcome under the chosen conditions (E_a too large). This is illustrated in Figure 17.3 where the reaction diagrams for

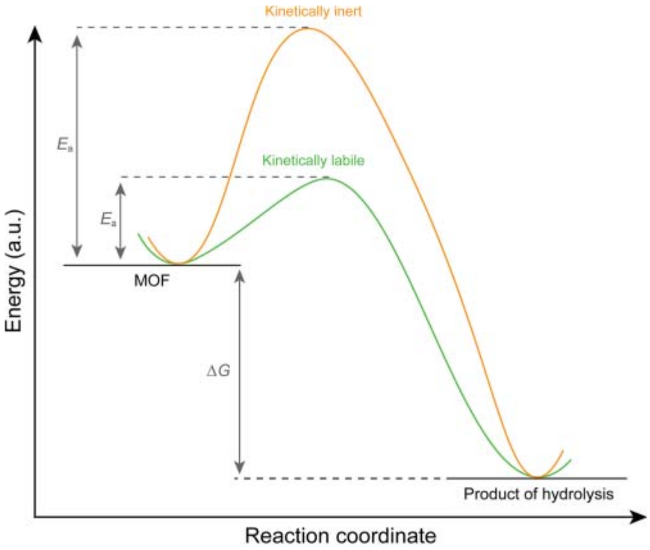

Figure 17.3 Comparison of the reaction diagrams of two thermodynamically unstable MOFs. In both cases the products of hydrolysis are thermodynamically favored (ΔG is negative). Kinetic inertness due to a high activation energy E_a (orange curve) results in an increased hydrolytic stability. Kinetic lability and the concomitant low activation energy for the hydrolysis renders the MOF unstable toward water (green curve).

the hydrolysis of two compounds with identical thermodynamic (in)stability but different kinetic lability are shown. For both compounds the hydrolysis is thermodynamically favored, but the difference in activation energy renders one of them hydrolytically more stable (orange curve) than the other (green curve).

There are multiple structural factors that can cause a MOF to be kinetically inert such as steric shielding of the SBU, rigidity of the SBU and/or the linker, the electronic configuration of the metal, and the hydrophobicity.

17.2.4.1 Steric Shielding

The most obvious way of introducing kinetic inertness is by steric shielding. This means that the attack of the thermodynamically unstable metal–linker bond by water is slowed down or prevented completely by the introduction of shielding moieties. This can be realized in three different ways: (i) SBUs with high connectivity, (ii) bulky linkers, and (iii) interpenetrating frameworks.

SBUs with high connectivity are frequently encountered in zirconium- and hafnium-based MOFs since these metals favor the formation of M_6O_8-core SBUs ($M = Zr^{4+}, Hf^{4+}$) with a maximum connectivity of 12 (Figure 17.4a). A prominent example is UiO-66 that is built from 12-c Zr_6O_8-core SBUs joined by ditopic BDC linkers to form a framework of **fcu** topology (see Figure 4.28) [7]. The high connectivity of the 12-c SBU endows UiO-66 with high hydrolytic stability by shielding through the binding groups of the linker. Other MOFs that are built from SBUs with high connectivity are hydrolytically stable, which confirms that steric shielding of the SBU by the binding groups is a viable approach for the design of water-stable MOFs [8]. Most of these SBUs are of the M_6O_8-type ($M = Zr^{4+}$, Hf^{4+}) or of rod-like nature and a selection is shown in Figure 17.4. The crowding

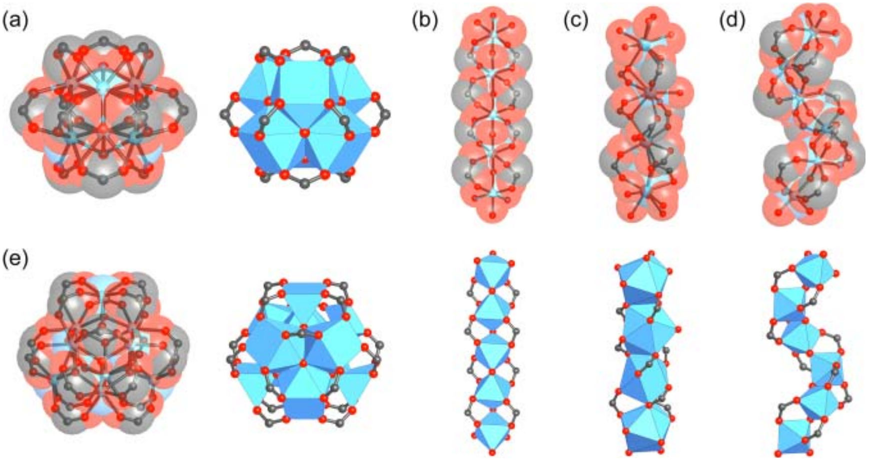

Figure 17.4 SBUs with high connectivity that endow MOFs with water stability due to steric shielding. Shown is a comparison of the polyhedral representation and the ball-and-stick representation overlaid with the corresponding space-filling model highlighting the steric shielding by the binding groups. (a) The most common SBU with high connectivity has the 12-c M_6O_8-core ($M = Zr^{4+}, Hf^{4+}$). Other SBUs include many rod-like SBUs such as that in (b) MIL-53, (c) La(BTB), or (d) CAU-10 as well as rare earth SBUs such as that of (e) **gea**-MOF-1. Color code: Metal, blue; C, gray; O, red.

of linkers around the SBU can prevent the formation of water clusters in close proximity and hinders water molecules from getting close to the metal centers as illustrated by the space-filling representation.

A second way to increase the kinetic inertness is the introduction of bulky substituents on the linker to sterically shield the SBUs. In contrast to the high connectivity of the SBUs discussed above, this is often possible by rational design of the linker. An example illustrating this approach is the functionalization of the BDC linker in DMOF ($Zn(BDC)(DABCO)_{0.5}$), a pillared-layered MOF built from 2D $Zn_2(BDC)_2$ **sql** layers that are pillared by DABCO linkers to form a **pcu** framework (Figure 17.5a) [9]. The zinc paddle wheel SBUs readily hydrolyze in the presence of water, leading to the structural degradation of DMOF [10]. An additional methyl substituents appended to the H_2BDC linker effectively shields the SBUs and the subsequent addition of further methyl groups permits systematic tuning of the kinetic water stability of DMOF derivatives [3]. While the additional methyl groups shield the SBUs, the increase in stability cannot be rationalized in terms of steric shielding alone but the increased hydrophobicity of DMOF derivatives has to be considered. Figure 17.5 gives a comparison of the pristine and modified DMOF, highlighting the shielding effect of the methyl substituents on the BDC linkers.

Interpenetration has as similar effect on the hydrolytic stability of MOFs, and the water stability of interpenetrated MOFs is consequently higher than that of their non-interpenetrated counterparts. Interpenetration of frameworks is

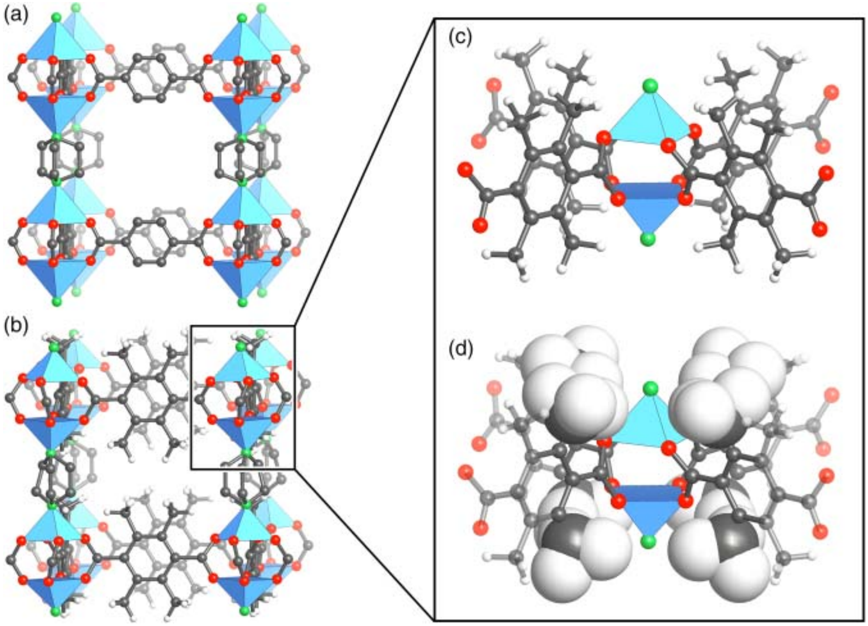

Figure 17.5 Crystal structure of (a) DMOF and (b) $(Me)_4$-DMOF (modeled based on DMOF). (c, d) Steric shielding effect of the methyl substituents on the $Zn_2(-COO)_4$ paddle wheel SBUs. Both the (c) ball-and-stick and (d) partial space-filling model are shown. The top and bottom of the paddle wheel SBUs are shielded by the DABCO ligands (omitted for clarity). Color code: Zn, blue; H, white; C, gray; N, green; O, red.

necessarily accompanied by a decrease in the pore size and pore volume, and thus results in lower uptake capacities. It is also important to remember that it is not necessarily possible to synthesize an interpenetrated counterpart for every MOF structure.

17.2.4.2 Hydrophobicity

Structural degradation by hydrolysis or linker displacement is a two-step process. In the first step, water clusters are formed near the SBU before the reaction of water and the metal centers in the SBU occurs and leads to the structural degradation of the MOF. The formation of water clusters near the SBU can be avoided in three ways: (i) Appending hydrophobic alkyl substituents to the linker to avoid the formation of water clusters close to the SBU through repulsive interactions. (ii) Introduction of polar functional groups such as amines and alkoxy groups that draw water away from the SBU and act as basins of attraction. (iii) Fluorination of the linker to give hydrophobic MOFs that repel water [11]. Even though the last approach is the most effective one, it eliminates the possibility for water adsorption to occur because water cannot permeate the surface of the MOF. Introducing alkyl chains or polar groups provides a more reasonable approach since both allow water to enter the pore system while minimizing the likelihood of hydrolysis. Introducing additional functional groups into the pores of the framework lowers the maximum capacity, and the nature of the functionalities has a dramatic impact on the position of the inflection point of the isotherm.

17.2.4.3 Electronic Configuration of the Metal Center

The electronic configuration of the metal centers in the SBUs can endow a thermodynamically unstable MOF with kinetic inertness. This concept is well established for transition metal complexes. Here we will illustrate this for octahedrally coordinated metal centers in $M_3OL_3(COO)_6$ SBU (Figure 17.6). Findings based on these considerations cannot be transferred directly to other structures where the coordination geometry of the metal is different which, according to the ligand field theory, leads to a different splitting of the d-orbitals. MIL-101 can be prepared from a variety of trivalent metals such as Cr^{3+}, Fe^{3+}, and Ti^{3+}. For coordination by carboxylate binding groups (i.e. R–COO^-) and

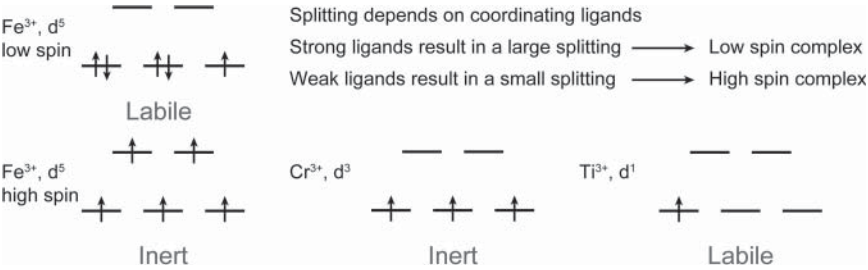

Figure 17.6 Electronic configuration of d-elements that are often used to construct the SBUs of MOFs. The weak field ligands typically present in MOFs (e.g. O^{2-}, OH^-, and R–CO_2^-) lead to a small ligand field splitting and high spin complexes. Asymmetric occupation of the orbitals (e.g. Ti^{3+} L.S.) renders the resulting complexes kinetically labile, whereas a symmetric occupation (e.g. Fe^{3+} and Cr^{3+} L.S.) results in kinetic inertness.

other weak field ligands (e.g. HO^-, H_2O) a high-spin configuration is expected. Cr^{3+} has a d^3 configuration, and according to Hund's rules all d-electrons are located in the t_{2g} orbitals. Therefore, (Cr)MIL-101 is kinetically inert. In the case of the d^5 ion Fe^{3+} every d-orbital is occupied by one electron and this symmetric occupation of d-orbitals renders Fe^{3+} kinetically inert. Things are different for Ti^{3+}. The d^1 configuration of Ti^{3+} results in a single d-electron occupying the degenerated t_{2g} orbitals. Such an asymmetric occupation of d-orbitals is kinetically labile. Even though this principle is very simple it can give qualitative information regarding the kinetic inertness of MOFs. A comparison of (Al, Cr)MIL-53, ((Al,Cr)(OH)(BDC)), and (V)MIL-47 (V(O)(BDC)), three isostructural **sra** frameworks, reveals that chemical stability follows the order $Cr^{+3} > Al^{+3} > V^{+4}$, a finding that is in good agreement with the decreasing inertness $Cr^{+3} > Al^{+3} > V^{+3} > V^{+4}$. In contrast, the bond strength (thermodynamic stability) of the M—O bond (calculated for the corresponding oxides) follows the reverse order V > Al > Cr [12]. This illustrates how kinetic inertness defines the stability toward water whereas the strength of the metal–linker bond is not always an appropriate indicator for the hydrolytic stability but always defines the thermal stability. The outstanding water stability of (Cr)MIL-53 originates not only from the kinetic inertness of Cr^{3+} but also from the large difference in the energy of the frontier orbitals of Cr^{3+} and water.

17.3 Water Adsorption in MOFs

17.3.1 Water Adsorption Isotherms

Vapor sorption is in many ways different from that of gases. The shape of water vapor adsorption isotherms gives direct information on the hydrophilicity or hydrophobicity of hydrolytically stable MOFs. Isotherms of MOFs that are not hydrolytically stable do not allow gaining such information because their shape is governed by the chemical nature of their decomposition products rather than that of the MOF itself. Hydrophilic materials show strong affinity to water molecules, a definition that cannot be directly applied to porous materials. Hydrophobic mesoporous silica (e.g. MCM-41 and SBA-15) adsorb more water than most more hydrophilic microporous zeolites. This finding is explained by the fact that the adsorption of water is largely dictated by the pore size. Therefore, the hydrophilicity of a given MOF is commonly determined by its selectivity for water over other components in a mixture. The position of the inflection point (α) on the water sorption isotherm is often used to determine the relative hydrophilicity. The inflection point is defined as the point at which half of the maximum uptake is reached. Figure 17.7 shows the isotherms of four materials ranging from strongly hydrophilic to strongly hydrophobic (a through d). Isotherm (a) has the shape of a typical Type I isotherm. Water is adsorbed at very low relative pressures and the maximum loading is therefore also reached at low relative pressures. The corresponding Henry's constant (slope at pressures close to $P/P_0 = 0$) is large and the inflection point is located at very low relative pressures. Isotherm (b) shows a smaller slope at low relative pressures and resembles a Type II or Type IV isotherm; hence the corresponding MOF is less hydrophilic than that leading to isotherm (a). Adsorbent (c) shows

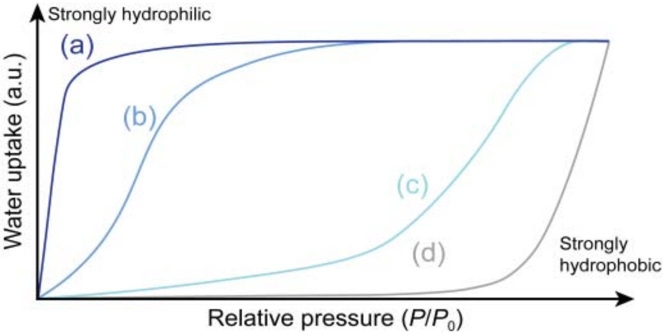

Figure 17.7 Schematic isotherms for (a) microporous strongly hydrophilic, (b) microporous less hydrophilic, (c) mesoporous "hydrophilic," and (d) strongly hydrophobic MOFs.

resembles a Type III isotherm. The uptake at low relative pressures is very low and is explained by the formation of clusters rather than a monolayer. The uptake eventually reaches the same maximum uptake as in cases (a) and (b) but at considerably higher relative pressures, which is indicative of a relatively hydrophobic pore system. The similar maximum capacity for (a)–(c) indicates similar pore volumes for all three materials while the different inflection points can be used as a relative measure of the hydrophilicity. A linear isotherm with a constant small slope like that shown in (b) is commonly observed for strongly hydrophobic materials, and in this case an uptake is only observed close to or at the saturation vapor pressure. It should be noted, that a comparison of the relative hydrophilicity/hydrophobicity of pore systems is strictly speaking only possible if the pore size and the dimensionality of all compared pore systems are identical (e.g. functionalized derivatives of the same MOF).

The adsorption of water in MOFs can occur following three main mechanisms. Structural factors such as the pore size and the nature of the primary adsorption sites influence which of these three mechanisms is observed and they are the subject of the Section 17.3.2.

17.3.2 Mechanisms of Water Adsorption in MOFs

17.3.2.1 Chemisorption on Open Metal Sites

Open metal sites are a frequently encountered structural motif in MOFs. They are formed by the removal of terminal neutral ligands (e.g. water, solvent) from the coordination sphere of the SBU in MOFs such as paddle wheel (e.g. HKUST-1) and many rod-like SBUs (e.g. MOF-74). In contrast to HKUST-1, which, similar to other MOFs constructed from copper paddle wheel SBUs, displays low stability in the presence of water, (M)MOF-74 (M = Zn, Ni, Co) shows a relatively high hydrolytic stability.[1] The structure of (M)MOF-74 is built from helical rod SBUs that are connected by H_4DOBDC linkers to form

---

[1] Loss of terminal water from the SBUs is known for many rod-like and discrete SBUs (e.g. di- and trinuclear paddle wheel, $M_3O(H_2O)_2(COO)_6$, $Cu_3O(OH)(H_2O)_2(Py)_3$, $[M_3(-O)_3(H_2O)_3(COO)_3]_\infty$). The dehydration of the $Zr_6O_4(OH)_4(-COO)_{12}$ SBUs in UiO-66 follows a significantly different mechanism. Upon heating to temperatures above 250 °C the SBU loses four bridging –OH groups, which decreases the coordination number of Zirconium from 8 to 7 and results in a distortion of the cluster [13].

frameworks of **etb** topology with hexagonal 1D channels of approximately 11 Å that run along the crystallographic *c*-axis. Each pore is bordered by six SBUs with neutral water ligands bound to the metal centers that point into the center of the pore. Those terminal water ligands are removed by heating in dynamic vacuum, leaving behind open metal sites. Density functional theory (DFT) calculations for fully activated (Mg)MOF-74 show that a large unoccupied orbital is located at those open metal sites, making them strong Lewis acids [14]. Single-crystal X-ray diffraction studies on hydrated (Zn)MOF-74 show the different nature of the water species adsorbed in the framework. Figure 17.8a shows one pore of (Zn)MOF-74 with a view along the *c*-direction where all adsorbed water molecules are represented by their thermal ellipsoids [15]. Three different species can clearly be distinguished. The water coordinated directly to the SBU is bound strongly, which is reflected in small thermal ellipsoids. A second layer of water is adsorbed close to the SBUs. The strong physisorption interaction between these water molecules and the framework is weaker than that for chemisorption on the open metal sites and consequently the thermal ellipsoids for these water molecules are larger. Finally, weakly bound water molecules are located at the center of the pore. Figure 17.8c shows the different dehydration

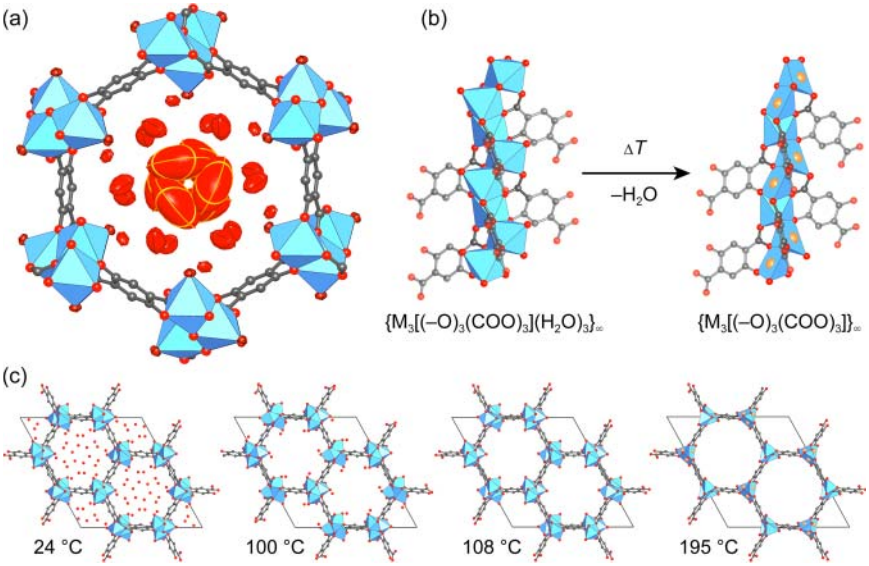

Figure 17.8 (a) One pore of hydrated (Zn)MOF-74 with view along the crystallographic *c*-axis. Three species of adsorbed water can be distinguished: (i) chemisorbed water on the open metal sites of the SBU, (ii) strongly physisorbed water close to the SBU, and (iii) loosely bound water at the center of the pore. All oxygen atoms of water are shown as their respective thermal ellipsoids (50%). (b) Segments of the SBU of (Zn)MOF-74 in its hydrated (left) and dehydrated (right) states; open metals sites are highlighted in orange. (c) Dehydration steps of (Zn)MOF-74 at different temperatures. Water located in the center of the pores is lost at 100 °C, water physisorbed close to the SBUs at 108 °C, and water chemisorbed on the open metal sites at 195 °C. All hydrogen atoms are omitted for clarity. Color code: octahedral Zn, blue; Zn open metal sites, orange; C, gray; O, red.

steps and Figure 17.8b shows fragments of the hydrated and dehydrated SBU of MOF-74. The high temperature required to regenerate MOF-74 to its full capacity is related to the strong binding of water to open metal sites, which is undesirable for most applications. It should also be pointed out that adsorption and desorption of water on open metal sites leads to global or local deformation of the structure, which can often result in gradual structural degradation.

The presence of open metal sites typically results in adsorption of water at low relative pressures (P/P_0) leading to Type I isotherms and a large Henrys constant K_H (slope of the isotherm at $P/P_0 \rightarrow 0$). A steep uptake at very low P/P_0 and a hysteresis (i.e. a discrepancy between the adsorption and desorption branch) in the low-pressure region of the isotherm is indicative of chemisorption. With respect to applications, this means that a high energy input is needed to restore the full capacity of such MOFs. Therefore, in many cases MOFs that adsorb water reversibly and require less energy for the complete regeneration of their capacity are more desirable.

17.3.2.2 Reversible Cluster Formation

The adsorption of water by reversible formation of water clusters is a mechanism commonly observed for porous carbons, and a similar mechanism has been observed for microporous MOFs such as MOF-801 ($Zr_6O_4(OH)_4$(fumarate)$_{12}$) [16]. MOF-801 is built from 12-c Zr_6O_8-core SBUs and fumarate linkers that are connected to form an **fcu** net that features two differently sized tetrahedral and one octahedral pore with diameters of 4.8, 5.6, and 7.4 Å, respectively (Figure 17.9a) [8e, 17]. The bridging –OH groups on the $Zr_6O_4(OH)_4(-COO)_{12}$ SBUs of MOF-801 are the primary adsorption sites. At low relative pressures water is adsorbed by hydrogen bonding to these –OH groups, which leads to the formation of tetrahedral water clusters within the small tetrahedral pores (Figure 17.9c). At higher relative pressures additional water molecules are confined within the tetrahedral pores and consequently a body-centered cubic water cluster is formed (Figure 17.9d). At even higher relative pressures, adsorption in a similar arrangement is observed for the octahedral pores (Figure 17.9b). The octahedral pores do not feature primary adsorption sites; however, water molecules adsorbed in the tetrahedral pores provide adsorption sites that facilitate the adsorption of water in the larger cavity of the framework. This leads to the formation of larger water clusters that eventually connect, which results in continuous pore filling. The different adsorption sites in the tetrahedral and octahedral pores of MOF-801 are shown in Figure 17.9.

Cluster-mediated adsorption has the advantage that a large working capacity in applications based on adsorption/desorption using mild temperature- and pressure swing adsorption (TSA and PSA) can be achieved. A cluster-mediated pore-filling mechanism can only occur for porous materials with pore diameters $<D_c$, the critical pore diameter for capillary condensation. The critical diameter for capillary condensation of water is 20.76 Å (at 25 °C) and can be calculated following Eq. (17.1):

$$D_c = \frac{4\sigma T_C}{(T_C - T)} \tag{17.1}$$

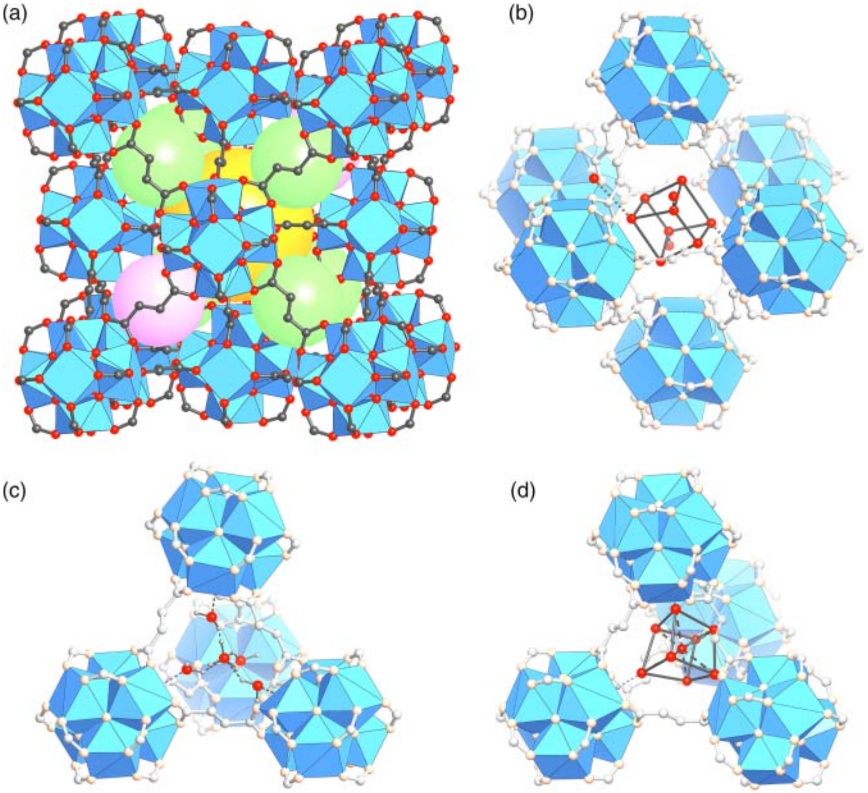

Figure 17.9 (a) Single-crystal structure of MOF-801. The pink, green, and yellow spheres highlight the small tetrahedral (4.8 Å), large tetrahedral (5.6 Å), and octahedral (7.4 Å) pores, respectively. (b)–(d) Three different water clusters are formed in the three distinct pores. (b) A cubic cluster is formed in the octahedral, (c) a tetrahedral cluster in the small tetrahedral, and (d) a body-centered cubic cluster in the large tetrahedral pore. All hydrogen atoms are omitted for clarity. Color code in (a): Zr, blue; C, gray; O, red. Color code in (b–d): Zr, blue; C, and O atoms that are part of the framework are shown in white and light orange, respectively, and the oxygen atoms of adsorbed water are shown in red.

where σ is the van der Waals diameter of the adsorbent and T_C and T are the critical temperature of the adsorbate and the adsorption temperature, respectively. Based on this, a large working capacity for microporous materials within the range of 10–30% RH is expected for materials with large pore volumes and pore sizes approaching this limit. The structure of Co_2Cl_2(BTDD), a MOF built from infinite helical SBUs that are connected through linear ditopic BTDD linkers, is composed of hexagonal channels with a diameter just above the critical pore diameter for capillary condensation of water (about 21 Å) for the fully activated MOF (Figure 17.10a) [5]. Hydration at low relative pressures results in occupation of the open metal sites by water (Figure 17.10c), which decreases the pore diameter to about 17 Å leading to a microporous material (Figure 17.10b). Therefore, the water adsorption isotherm of Co_2Cl_2(BTDD) is of Type IV and shows a steep uptake at low relative pressures

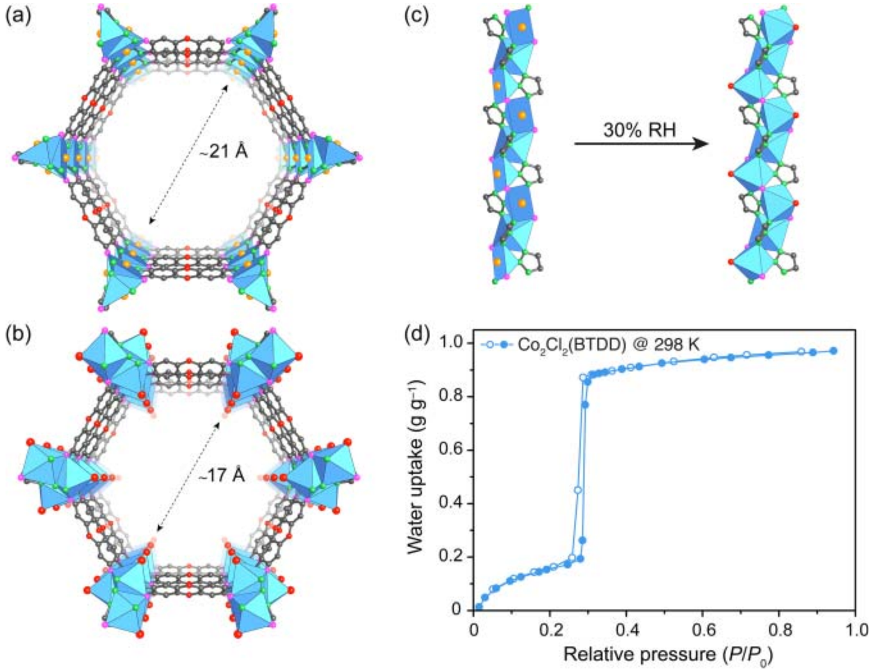

Figure 17.10 Crystal structure and water adsorption isotherm of Co_2Cl_2(BTDD). (a) One pore of fully activated Co_2Cl_2(BTDD) with view along the crystallographic *c*-axis. The fully activated structure features open metal sites pointed at the center of the pore. The pore diameter is about 21 Å, which is above the critical diameter for capillary condensation (D_c = 20.76 Å at 25 °C). (b) Adsorption of water on the open metal sites results in a decrease of the pore diameter to the microporous regime (about 17 Å). (c) Illustration of the hydration of the open metal sites on the SBUs of Co_2Cl_2(BTDD) at 30% RH. (d) Water adsorption isotherm of Co_2Cl_2BTDD recorded at 298 K. The low inflection point (α) at $P/P_0 = 0.29$ indicates a hydrophilic pore surrounding. Color code: octahedral Co, blue; Co open metal sites; orange; C, gray; N, green; O, red; Cl, pink.

(inflection point $\alpha = 0.29$), almost no hysteresis, and a maximum capacity of $q_{\max} = 0.97\,\mathrm{g\,g^{-1}}$ (Figure 17.10d). The large water uptake and the low inflection point are a result of the polar and hydrophilic nature of the BTDD linker, the large pore volume, and the pore diameter close to D_c. High initial Q_{st} values at low coverage indicate strong interactions between water and the framework, while Q_{st} values during pore filling (~44 kJ mol^{-1}) drop close to the evaporation enthalpy of water (−40.7 kJ mol^{-1}), indicating that in this pressure window water–water interactions are predominant.

17.3.2.3 Capillary Condensation

For MOFs with pore diameters larger than D_c the adsorption of water on primary adsorption sites or in the shape of mono-/multilayers is followed by capillary condensation. In contrast to the cluster-mediated filling in hydrophilic microporous MOFs, adsorption by capillary condensation in mesoporous MOFs is irreversible and results in Type IV and V isotherms that typically show a hysteresis loop (Figure 17.11). An example for a MOF showing this type of adsorption behavior

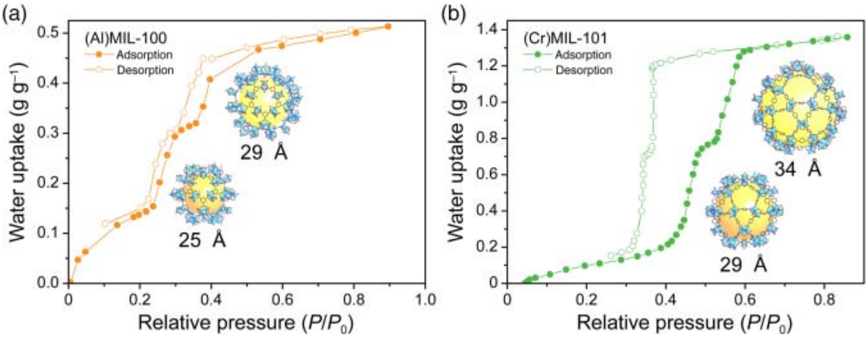

Figure 17.11 Typical water adsorption isotherms of mesoporous MOFs. An S-shaped isotherm and hysteresis are indicative of capillary condensation. The presence of two differently sized cages in the **mtn** type structures of (a) MIL-100 and (b) MIL-101 lead to two distinct steps in the corresponding adsorption isotherms. The adsorption is represented by filled symbols, the desorption by open symbols. All hydrogen atoms are omitted for clarity. Color code: Al and Cr, blue; C, gray; O, red.

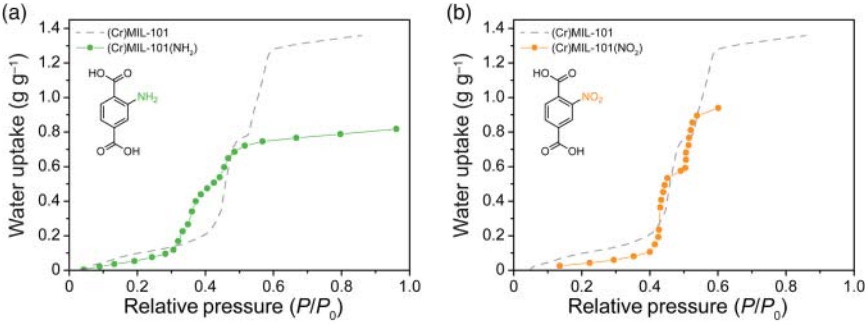

Figure 17.12 Influence of differently substituted BDC linkers in the structure of (Cr)MIL-101 on the water adsorption isotherm. (a) Functionalization with amine groups (–NH_2) renders the pores more hydrophilic and therefore shifts the inflection point to lower relative pressures. The decreased pore volume lowers the maximum adsorption capacity. (b) Hydroneutral nitro (–NO_2) substituents have a less pronounced effect on the inflection point; however, a decrease in the maximum capacity is observed. In both cases, the general shape of the isotherm is retained and the adsorption isotherm of pristine (Cr)MIL-101 is shown in gray.

is MIL-101. The **mtn** type structure of MIL-101 contains three differently sized cages, two of which are in the mesoporous regime and measure 29 and 34 Å in diameter (see Figure 4.12). The adsorption isotherm has the typical S-shape, showing low uptake at low relative pressures, a steep uptake at around $P/P_0 = 0.4$, and a second steep uptake at $P/P_0 = 0.5$ that are correlated to filling of the 29 and 34 Å large cages, respectively (Figure 17.11b) [18]. The adsorption is initiated by nucleation and growth on the inner surface, which is followed by capillary condensation at higher pressures that results in a hysteresis loop. This also manifests itself in the heats of adsorption determined at different coverage. The high heat of adsorption (about $-80\,\mathrm{kJ\,mol^{-1}}$) at low coverage is due to strong interactions of the open metal site with water, whereas a coverage of about 20%, Q_{st} decreases by almost 50% (about -45 to $-50\,\text{kJ mol}^{-1}$), which is in the same range as the evaporation enthalpy of water (about $-44\,\text{kJ mol}^{-1}$) [19].

17.4 Tuning the Adsorption Properties of MOFs by Introduction of Functional Groups

Functional groups can have a significant effect on the shape of the adsorption isotherm, the position of the inflection point, and the maximum uptake. The general shape of the isotherm is governed by the hydrophilicity/hydrophobicity (see Figure 17.7), pore diameter, and chemical nature of the adsorbent such as the presence of open metal sites. Hydrophilic MOFs with pore diameters <20 Å typically show S-shaped isotherms unless their structures contain open metal sites, in which case Type I isotherms are observed. Multiple adsorption steps common for structures with hierarchical pore systems and hysteresis are observed for mesoporous MOFs or MOFs with open metal sites. Aside from the presence of open metal sites, the abovementioned parameters cannot be altered for a given material. In contrast, this is possible for the hydrophilicity that can be altered by introducing functional groups onto the backbone of the linker. To illustrate the effect of different functional groups on the adsorption properties of MOFs we consider a series of functionalized (Cr)MIL-101 analogs. The water adsorption of pristine (Cr)MIL-101 has been discussed earlier and its adsorption isotherm is shown in Figure 17.11b. The influence of chemical modifications of the BDC linker by appending functional groups such as $-NO_2$ and $-NH_2$ groups reveals trends that are applicable to other MOFs [18, 20]. The relative pressure at which the inflection point of the isotherm is observed can act as an indicator for the hydrophobicity. The inflection point is shifted to lower relative pressures for $-NH_2$ functional groups, whereas $-NO_2$ groups seem to have a negligible effect on the position of the inflection point. In general, hydrophilic groups (e.g. $-NH_2$, $-OH$) shift the inflection point to lower pressures, hydroneutral groups (e.g. $-COOR$, $-COR$) have no effect on the position of the inflection point, and hydrophobic groups (e.g. $-F$, $-CH_3$) shift it to higher values. The classification of functional groups as hydrophilic, hydroneutral, and hydrophobic is based on their donor- and hydration number rather than the dipole moment [21]. In all three cases, the free pore volume is decreased by the additional substituent protruding into the pores, which leads to a lower maximum uptake. While the pressure at which capillary condensation occurs strongly depends on the chemical nature of the substituents appended to the linker, the desorption pressure is nearly unaltered. This is explained by the fact that the hydrophilic surface of (Cr)MIL-101(NH_2) is covered with adsorbed water at lower relative pressures, thus allowing for capillary condensation to take place at lower relative pressures. In the desorption step the pore size is the deciding factor, which is approximately the same for all three MOFs.

The principles discussed above are generally applicable and similar modifications carried out on other MOFs result in similar effects. Amino functionalization of the *m*-BDC linker in CAU-10 even results in a transition from a Type V to Type

I isotherms. In contrast, appending nonpolar hydrophobic groups such as $-CH_3$ result in a significant shift of the inflection point to higher relative pressures [22].

Functionalization of linkers can also influence the “breathing” behavior of MOFs. While breathing of MOFs in the presence of CO_2 is well studied only few examples of breathing initiated by the adsorption of water are known. Pristine (Al)MIL-53 shows no breathing in the presence of water, while (Al)MIL-53(OH) and (Al)MIL-53(NH_2) undergo structural change at high RH values [23]. The step around RH 80% in the water adsorption isotherm of (Al)MIL-53(OH) corresponds to a phase transition from the narrow pore (*np*) to the wide pore (*wp*) phase and results in a fivefold increase of the water uptake. This phenomenon may be explained by stronger interaction between –OH groups and water compared to the other isoreticular MOFs.

17.5 Adsorption-Driven Heat Pumps

Heating and cooling systems find widespread application in industry as well as in our daily lives. Such systems are mostly of mechanical nature due to comparatively low production costs and high coefficient of performance values [24]. Some major drawbacks of mechanical systems are that they consume large quantities of energy and rely on liquid refrigerants that have detrimental effects on the environment such as the depletion of the ozone layer and global warming [25]. While the use of chlorofluorocarbons and hydrochlorofluorocarbons as refrigerants has been prohibited, first by the Montreal agreement in 1988 and later in the Kyoto agreement in 1998, respectively, hydrofluorocarbons are still widely used [25c]. Therefore, the development of alternative technologies that operate with a higher energy efficiency and do not rely on the use of toxic refrigerant is sought after. For the evaluation of the efficiency for heat pump systems the primary energy efficiency must also be considered. Mechanical heat pumps operate using electrical power, which is generated in a separate process, thus lowering the overall efficiency. Today, absorption-driven heat pumps using salt solutions as the working liquid have found their way into many applications. Adsorption-driven heat pumps (ADHP) are based on the same working principle as their absorption-based counterparts but use a solid rather than a liquid adsorbent, making the devices more transportable and easier to handle. Furthermore, ADHPs can operate on different environmentally friendly primary energy sources such as solar energy, geothermal energy, or waste heat. Therefore, ADHPs represent an environmentally friendly alternative to mechanical heat pumps. In this section, the working principle of ADHPs is outlined and requirements regarding the vapor adsorption behavior of the adsorbent are discussed. ADHPs can operate on different working fluids (e.g. water, methanol, ethanol, and ammonia); here we will focus on water. A more detailed discussion of ADHPs is found in reference [1a].

17.5.1 Working Principles of Adsorption-Driven Heat Pumps

The concept of ADHPs may seem confusing at first since the overall process describes heat transfer from a reservoir of low temperature (T_1) to one of higher temperature (T_2). The second principle of thermodynamics seems to contradict this heat transfer, but in a closed cycle where multiple state functions change simultaneously, this is possible. The overall process in ADHPs is similar to that of their absorption-driven counterparts with the sole difference being that ADHPs rely on a solid adsorbent. In contrast to a liquid medium the solid adsorbent cannot be circulated, meaning that all four components ((i) adsorber, (ii) desorber, (iii) evaporator, and (iv) condenser) of the heat pump are of the same material. Therefore, an ADHP consists of only two compartments. It can be used for heating or cooling applications, depending on whether the released heat of adsorption or that consumed by evaporation of the working liquid is utilized. A simplified representation of the working cycle of an ADHP is given in Figure 17.13.

17.5.2 Thermodynamics of Adsorption-Driven Heat Pumps

The use of water as the working fluid in ADHPs has several advantages when compared to the working fluids used in mechanical heat pumps: (i) it is nontoxic, (ii) abundant and readily available, and (iii) has a high evaporation enthalpy (2500 kJ kg^{-1}). The only drawback is that a relatively low vapor pressure of 1.0–6.0 kPa must be used under cooling conditions. Other possible working fluids include short-chain alcohols (i.e. methanol or ethanol) or other small molecules (e.g. ammonia). While the Carnot cycle used in mechanical heat

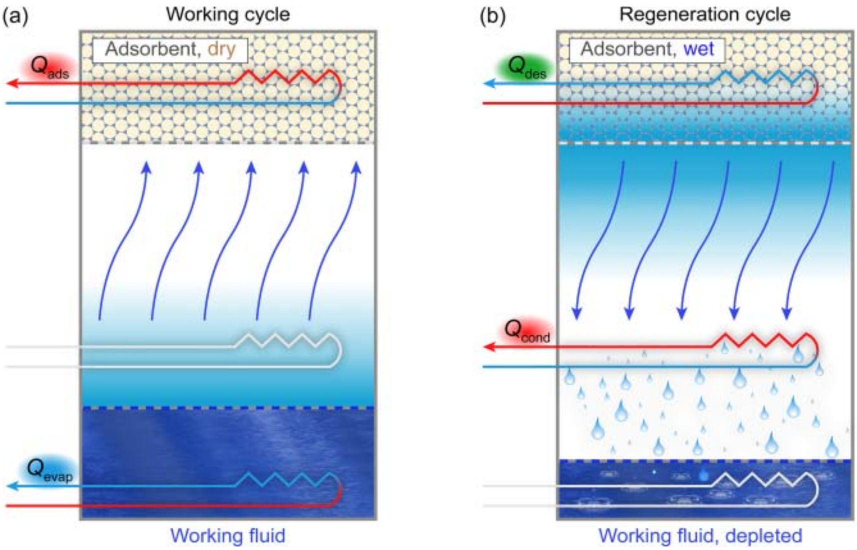

Figure 17.13 Working cycle and regeneration cycle of an adsorption-based heat pump. (a) Working cycle: the evaporation enthalpy $Q_{\text{evap.}}$ is consumed by the evaporation of the working fluid. The working fluid is then adsorbed by the adsorbent, leading to an increase in temperature due to the release of the heat of adsorption $Q_{\text{ads.}}$. (b) Regeneration cycle: desorption of the working fluid from the adsorbent is realized by heat transfer from an external source ($Q_{\text{des.}}$). The cycle is closed by the condensation of the liberated working fluid, which releases the heat of condensation ($Q_{\text{cond.}}$). Two applications are possible: (i) cooling ($Q_{\text{evap.}}$) or (ii) heating ($Q_{\text{ads.}} + Q_{\text{cond.}}$).

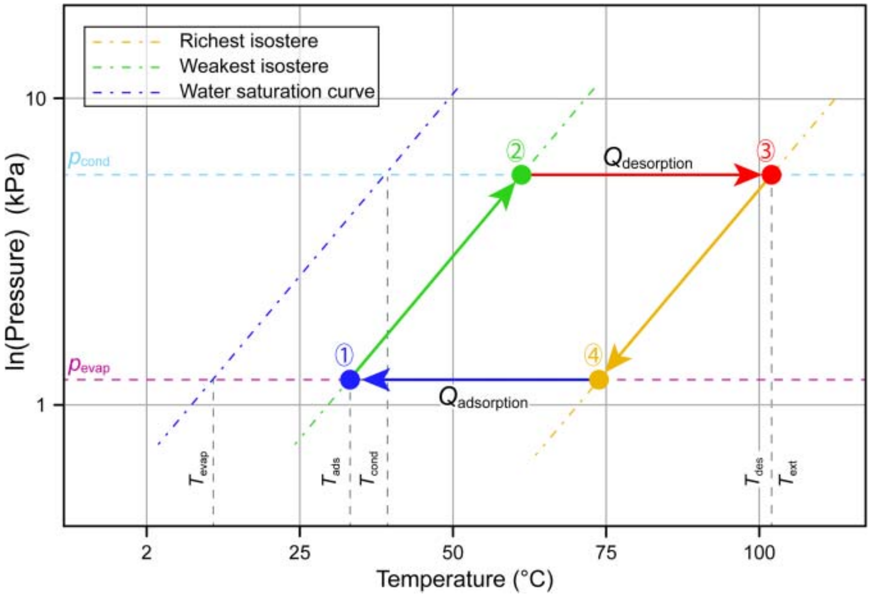

Figure 17.14 Arrhenius diagram for an adsorption-driven heat pump cycle. 4 → 1: Adsorption of the working fluid. 1 → 2: Isosteric compression. 2 → 3: Desorption by heat transfer from an external heat source. 3 → 4: Isosteric cooling.

pumps relies on two isothermal and two adiabatic compression and expansion steps, the four-step working cycle of ADHPs consists of two isosteres and two isobars. An isostere is a curve that describes a thermodynamic process involving adsorption in which the coverage does not change (i.e. constant loading, no ad- or desorption), and an isobar describes a thermodynamic process at constant pressure. The vertices of this cycle are defined by three temperatures: (i) the evaporator temperature (T_{evap}), the condenser temperature (T_{cond}), and the maximal desorption temperature (T_{des}, which is identical to the temperature of the external heat source T_{ext}). The condenser pressure (p_{cond}) and evaporator pressure (p_{evap}) can be deduced therefrom. For water, pressures of 1.2 and 5.6 kPa correspond to evaporation temperatures of 10 and 35 °C, respectively, appropriate temperature levels for cooling or low-temperature heating applications, respectively. Like any type of heat pump ADHPs operate in a discontinuous manner. The Arrhenius diagram of a full cycle is shown in Figure 17.14. It can be separated into two steps, the production and the regeneration step, that correspond to the adsorption and desorption of the working fluid, respectively. The working fluid exchange between these steps corresponds to the difference between the richest (4 → 1) and the weakest (2 → 3) isostere in the Arrhenius diagram.

The first step (4 → 1) is the production phase, where the working fluid is evaporated, cooling the system to T_{ads}. Isosteric heating (1 → 2) lifts the pressure level to the condenser pressure (p_{cond}). The desorption in the regeneration phase (2 → 3) is initiated by heat transfer from the external heat source until T_{ext}/T_{des} is reached. Different external heat sources that define the maximum desorption temperature are possible (e.g. solar thermal collector, geothermal, waste heat). Isosteric cooling (3 → 4) closes the cycle. The adsorption and desorption steps are isobaric processes; therefore, the suitability of MOFs for this application can be assessed by measuring the isotherms at p_{evap} and p_{cond} in the temperature intervals that correspond to steps 4 → 1 and 2 → 3. The temperature of the external heat source (T_{ext}) and the minimum adsorption temperature (T_{ads}) define the pressure window and thereby the reachable loading lift that is defined as the difference between the maximum loading (in $\mathrm{g_{water}\ g_{adsorbent}}^{-1}$) for the weakest and the richest isotherm.

For applications of heat pumps for domestic heating, MOFs that adsorb water at comparatively low relative vapor pressure are favorable. This is the case for highly hydrophilic microporous MOFs that typically show a steep uptake at low relative pressures. An uptake between 10% and 30% RH is desirable to have a strong affinity for water while regeneration is still facile. MOFs that adsorb water at high relative pressures can be used in thermally driven room chillers. Since the desorption process in thermally driven chillers is fueled by an external heat source (e.g. district or solar heating) a higher evaporator temperature is perfectly acceptable and a material with comparatively low affinity toward water is in fact desirable. Interesting examples of such materials are members of MIL-100 and MIL-101 family [18, 26]. With $1.37\ \mathrm{g\,g^{-1}}$, (Cr)MIL-101 has one of the highest water uptakes reported so far [27]. The areas of steep uptake are located between $P/P_0 = 0.3$ and 0.5. (Cr)MIL-101(NH_2) has a maximum lift of $0.55\ \mathrm{g\,g^{-1}}$. Many other MOFs and different working fluids have been evaluated for use in adsorption-driven heat pumps [1a, 28].

17.6 Water Harvesting from Air

Today, a large proportion of the world is experiencing water stress caused by climate change and the increasing world population, and a growing portion of the world's population is expected to be affected by water scarcity in the future [29]. Only 2.5% of the water on earth is fresh water and a mere 0.3% of this fresh water are directly accessible in rivers and lakes, whereas 30.8% are groundwater and 68.9% are locked up in glaciers. The remaining 97.5% are seawater and bringing it to drinking water quality by desalination using current technologies is energy intensive. To provide sufficient amounts of water, especially in areas with poor infrastructure, new technologies must be developed. Earth-s atmosphere contains large quantities of water – equivalent to about 10% of all fresh water resources – that can potentially be used to address the global water problem. About 13 000 trillion liters of water are estimated to be contained within the atmosphere in the form of vapor and droplets and efforts have been made to collect this water using two types of water collection devices: fog collectors/dew nets and sorption-based systems [30] (Figure 17.15). Fog collectors rely on dewing on fine nets to wick water from air. Even though they can be used in dry regions that receive less than 1 mm of rain per year, they do require fog and light winds to operate, which severely limits their application. Sorption-based systems operate in adsorption–desorption cycles. Here, the desiccant is saturated

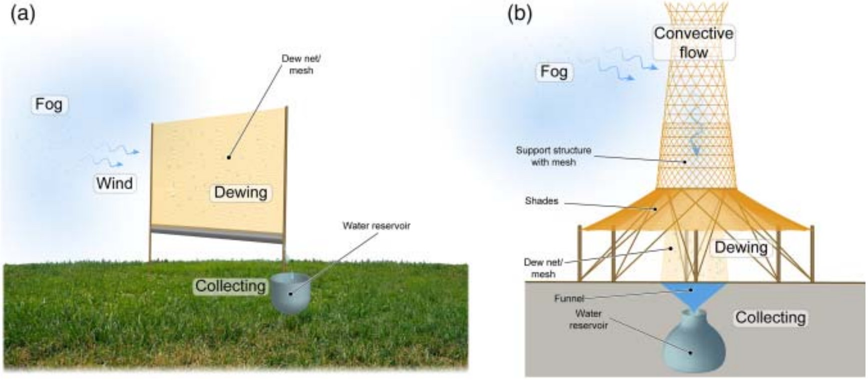

Figure 17.15 Schematics of two different concepts for fog collectors. (a) Illustration of a dew net. Air with 100% RH (fog) is transported to the dew net and consequently droplets form on the fine net. The droplets run down the net and are collected. (b) Tower for fog collection. In contrast to a dew net, the design of the tower sucks air to the mesh by convective air flow. Water droplets that form on the dew net run into a water reservoir.

with moisture under cold and humid conditions (during night) and desorption is achieved by heating (during the day). The desorbed moisture is then condensed, which requires a cold surface to reach the dew point for a given RH. Conventional desiccants such as $CaCl_2$ or silica gel show high water uptake at low RH, but due to the strong bonding of water to the desiccant a large amount of energy is required for its regeneration. This leads to low working capacities in autonomous devices.

Fog collectors require high humidity levels (close to 100% RH) to function, whereas the efficiency and viability of sorption-based water harvesting systems is limited by the adsorbent rather than the humidity levels. Therefore, the development of materials that can adsorb water at low RH and release it with minimum energy input is required. MOFs are interesting candidates for this application and we will illustrate the principles of water harvesting in autonomous low-energy devices and methods for the down-selection of promising materials.

17.6.1 Physical Background on Water Harvesting

To understand the requirements imposed on MOFs with respect to water harvesting applications it is instructive to consider the processes taking place within the water harvesting cycle. Figure 17.16a shows a schematic drawing of a water harvester [31]. The device consists of two main components: a case and a water sorption unit. The water sorption unit is a containment holding the MOF, and the case acts as an enclosure for the water sorption unit and as the condenser. To understand the processes within the device we need to consider the isotherms of the MOF and the psychometric chart for the given conditions. Figure 17.16b,c shows schematic isotherms at two different temperatures and a psychrometric chart between 0 and 65 °C at sea level, respectively. The water harvesting cycle starts with the saturation of the MOF at low temperatures and high RH during the night (I → ii, Figure 17.16b,c). Subsequent heating during the day leads to the

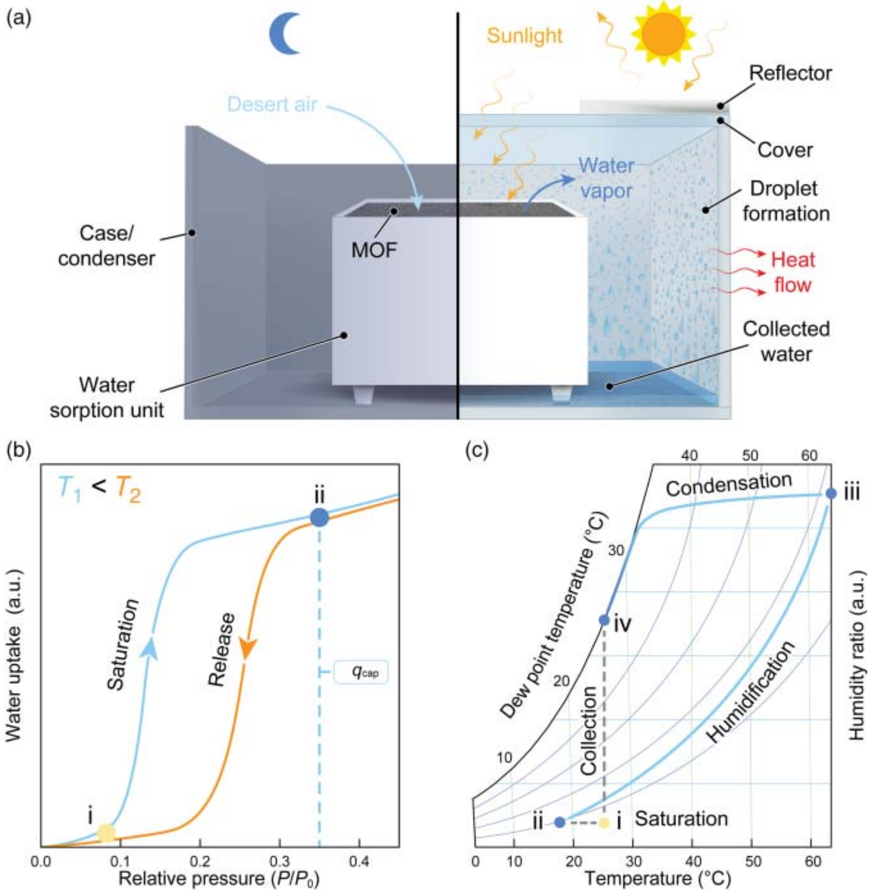

Figure 17.16 Working principles of a passive water harvester. (a) Schematic of a passive water harvester. At night the MOF is saturated (low temperatures, high RH). Solar thermal heating during the day leads to desorption of water and subsequent condensation on the cold surfaces of the case. (b) Schematic adsorption isotherms for two different temperatures ($T_1 < T_2$) illustrating the saturation with and release of water. (c) Schematic of the psychrometric chart at sea level. The temperature is plotted against the humidity ratio. An idealized water harvesting cycle is highlighted: starting at point i the MOF is saturated (overnight) until point ii is reached. A subsequent increase in temperature leads to desorption of water from the MOF that is accompanied by an increase in the humidity ratio until point iii is reached. When the humidified air is cooled at the condenser the dew point is reached and water vapor begins to condense (point iv).

desorption of water and a concomitant increase in the humidity ratio (ii → iii, Figure 17.16c). The water vapor is transported to the condenser by convection and cooled down to its dew point (iii → iv, Figure 17.16c). At the end of the day the condensed water is collected and the cycle starts over (iv → i, Figure 17.16c). To reach high efficiencies the MOF must fulfill the following requirements: high hydrolytic stability, adsorption of water at low RH, facile regeneration, high thermal conductivity, and high adsorption in the infrared range of the solar spectrum. The first three parameters can be adjusted by judicious choice of the building units and deliberate design of the MOF structure, whereas the latter two parameters can be enhanced by additives with good thermophysical properties (e.g. graphite) [32].

17.6.2 Down-selection of MOFs for Water Harvesting

Several factors are important in selecting a material for water harvesting applications: (i) the water stability, (ii) the cycling stability, (iii) the uptake capacity, (iv) the pressure and/or temperature swing response, and (v) the adsorption/desorption kinetics. Water stability and cycling stability have been discussed earlier in this chapter. Here, we will present a strategy for the down-selection of MOFs for water harvesting. This four-step process is illustrated in Figures 17.7 and 17.8. The first step is the determination of the water stability. For a water-stable MOF to be of interest for water harvesting applications, it should have a large uptake capacity. In addition to a large uptake the pressure window in which the uptake occurs and the location of the inflection point on the P/P_0 axis are important. A steep uptake in a narrow pressure region is advantageous since this will potentially allow for PSA within a narrow RH window. An inflection point at low pressures is favorable since it facilitates the saturation of the MOF at low RH. Figure 17.17a shows isotherms for three hypothetical materials. Only materials 1 and 2 are interesting candidates because they show a large uptake at low relative pressures within a narrow pressure window. Since the water harvesting process is a mixed PSA–TSA process, the temperature response of the material must be evaluated. For this purpose, isotherms at different temperature must be measured. An idealized set of isotherms for three different temperatures ($T_1 < T_2 < T_3$) is shown in Figure 17.17b. In this example, the inflection point is shifted significantly with temperature, which is desirable for efficient TSA cycles. The more pronounced

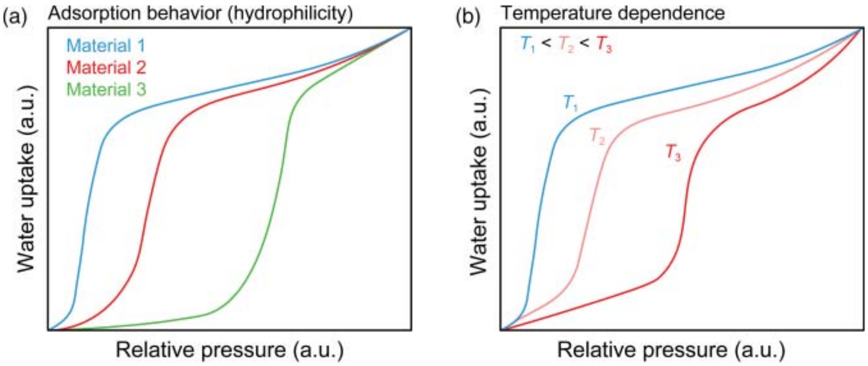

Figure 17.17 (a) Adsorption isotherms for materials of different hydrophilicity and pore dimensions. Material 1 is the most promising candidate because it shows a steep uptake at low relative pressures within a narrow pressure window. (b) Temperature-dependent water adsorption isotherms help analyze the temperature response and identify a reasonable temperature range for TSA.

the shift of the inflection point is at elevated temperatures, the more promising is the material.

The aforementioned measurements give idealized information on the adsorption properties under PSA and TSA conditions and represent equilibrium data. However, a kinetic component is always present, which leads to a lower usable working capacity for a defined cycle. Therefore, it is instructive to measure the kinetics of several adsorption–desorption cycles within different pressure and temperature intervals. Figure 17.18a shows an isotherm dissected into three pressure windows ($P_1 < P_2 < P_3$). These three segments have been chosen since it can be assumed that different adsorption mechanisms are predominant and therefore different kinetics are expected. Segment one is governed by monolayer adsorption, in segment two micropore filling dominates, and in segment three the diffusion is hindered and slows down the kinetics. The kinetics are determined by carrying out TGA (thermal gravimetric analysis) measurements either at constant temperature (Figure 17.18b, top right) or at constant RH (Figure 17.18b, bottom right). In both PSA and TSA experiments, material 1 shows faster kinetics and a larger maximum working capacity (MWC) for the selected TSA or PSA conditions. The working capacity within the water harvesting device is inevitably lower than the MWC determined in these experiments due to the influence of large-scale synthesis, processing and shaping of the material, limitations due to the design, and the specific cycling conditions. The kinetics determined in such measurements are strongly dependent on the synthesis and processing (e.g. powder, thin film, pressed pellets, or extrudates) of the MOF. Measurements of powders of different materials with the same packing density yield comparable results, and such measurements are inevitable for the proper evaluation of water adsorption materials.

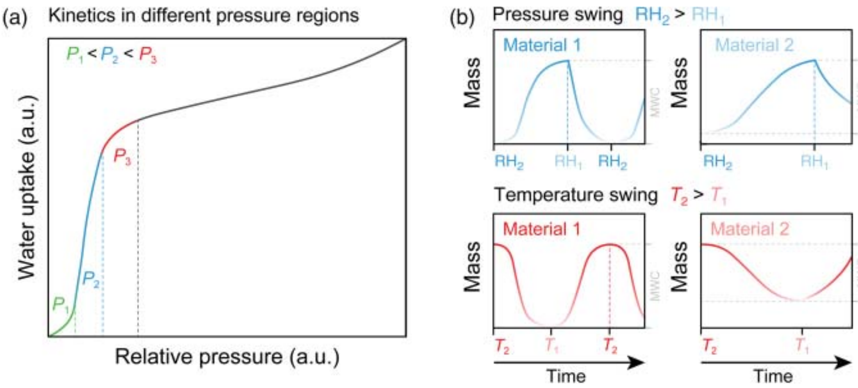

Figure 17.18 (a) Determination of the kinetics of water adsorption. Three segments of the isotherm are selected for TSA and PSA measurements. Those segments are selected based on the assumption that different mechanisms predominate in these pressure regions. (b) Pressure swing and temperature swing experiments help to further characterize the material and determine its suitability for water harvesting applications. Fast kinetics and a large working capacity are favorable.

17.7 Design of MOFs with Tailored Water Adsorption Properties

So far, we discussed different structural factors that have profound impact on the hydrolytic stability, the water adsorption mechanism, and the shape of the water sorption isotherm of MOFs [33]. In the following we will outline design principles for MOFs with tailored water adsorption properties. We will focus on influential structural parameters that are accessible by means of reticular chemistry and allow the adjustment of the water adsorption properties of MOFs.

17.7.1 Influence of the Linker Design

The hydrophilicity is the most influential physical parameter of the linker molecule with respect to the water adsorption properties of a MOF built therefrom. Hydrophilicity is a quantity that is not easily accessible. It is important to understand that the polarity of a given organic molecule does not necessarily correlate with its hydrophilicity. Nonpolar molecules are always hydrophobic, whereas polar molecules can be hydrophilic (e.g. $R–NH_2$, R–OH, and R–COOH), hydroneutral (e.g. $R–NO_2$, R–COR, R–COOR), or hydrophobic (e.g. R–Cl, R–F). As a rule of thumb, molecules that act as hydrogen bond donors or acceptors are hydrophilic. For potentially hydrophilic molecules the ratio between the overall exposed surface (van der Waals surface, A_{vdW}) and the polar surface (A_{polar}) helps rank their relative hydrophilicity as well as that of a pore system arising from its reticulation into a MOF. Introduction of heteroatoms capable of strong hydrogen bonding interactions render pore environments more hydrophilic. This principle is highlighted by the shift of the inflection point of the isotherm of CAU-10 analogs that are built from a variety of different linkers. Because all materials are of the same general structure, the shift of the inflection point is solely due to differences in the hydrophilicity of the linker (Figure 17.19). While appending hydrophilic functionalities to a linker molecule shifts the inflection point of the isotherm to lower relative pressures, in contrast to heterocyclic hydrophilic linker molecules, typically this is accompanied by a decrease of the maximum capacity, which is related to the decrease of the free pore volume.

17.7.2 Influence of the SBU

High valence metals lead to strong bonding with the organic linker and therefore the resulting frameworks are generally hydrolytically stable. Since a high atomic weight lowers the gravimetric capacity, the use of lighter elements such as aluminum or titanium, as compared to zirconium or hafnium, is favorable. In many MOF structures the bridging –OH groups in the SBUs act as primary adsorption sites by hydrogen bond formation with adsorbed water molecules [8e, 34]. Other primary adsorption sites with even stronger interaction (chemisorption) such as open metal sites result in Type I isotherms and hysteresis. In the context of large-scale applications, apart from the physical properties and the structural diversity associated with the use of certain metals their toxicity must also be considered. This is not only linked to health risks during the synthesis, but in the case of materials used for water harvesting applications, partial dissolution of the MOF results in the contamination of the harvested water. Therefore, when targeting materials for this application, the use of linkers and metals with a high LD_{50} is preferable (see Chapter 16) [35].

17.7.3 Influence of the Pore Size and Dimensionality of the Pore System

As illustrated in this chapter by several examples, different pore sizes lead to completely different adsorption mechanisms and isotherms. While microporous materials typically show S-shaped isotherms, an inflection point at comparatively low RH values, and no hysteresis, mesoporous materials with a pore diameter larger than $D_c = 20.76$ Å (at 25 °C) generally show pronounced hysteresis and an inflection point at high relative pressures. Consequently, microporous materials are favorable for water harvesting from air.

While it is difficult to quantify the influence of the dimensionality of the pore system, the magnitude of its effect on the adsorption properties is estimated to be rather small. To illustrate this hypothesis, we compare two structures with similar pore sizes and volumes but a different dimensionality of the pore system: (i) MOF-810 with a 3D pore system (**fcu** topology) and pore diameters between 4.8 and 7.4 Å and (ii) CAU-10 ($Al(OH)(m\text{-}BDC)$) with a 1D pore system (**yfm** topology) and pores of 7 Å diameter. Both structures have a similar pore volume ($V_p = 0.45$ and $0.43\ cm^3\ g^{-1}$, respectively), and bridging –OH groups of the SBUs are identified as the primary adsorption sites. The structural similarities outweigh the difference in the dimensionality of the pore system, as illustrated by similar inflection points (0.08 and 0.15, respectively) and maximum capacities ($q_{max} = 0.36\ g\ g^{-1}$) [8e, 36b].

17.7.4 Influence of Defects

In contrast to gas adsorption isotherms, water adsorption isotherms are very sensitive to the presence of defects in the crystal structure of the MOF. The shape of nitrogen and argon isotherms as well as the surface areas determined therefrom show only slight changes for high defect concentrations, whereas a significant shift of the inflection point as well as a higher adsorption capacity are commonly observed for the adsorption of water in such materials. The presence of defects in MOF-801 and UiO-66 (see Figure 4.28) renders their pores more hydrophilic and the larger pore volume leads to an increased maximum water uptake [8e, 37]. The presence of defects also manifests itself in the Q_{st} values calculated from water sorption isotherms. Q_{st} values at low coverage for defect-free UiO-66 are low ($Q_{st} = -15\ kJ\ mol^{-1}$) and increase with higher loading ($Q_{st} = -60\ kJ\ mol^{-1}$). In contrast, the Q_{st} values determined for defect-rich UiO-66 are significantly higher for low loading (-60 to $-70\ kJ\ mol^{-1}$). This is indicative of strong interactions between adsorbed water and the framework and consequently of hydrophilic pores. The presence and concentration of defects can significantly change the water adsorption behavior, which makes this method a valuable tool for the in-depth characterization of MOFs.

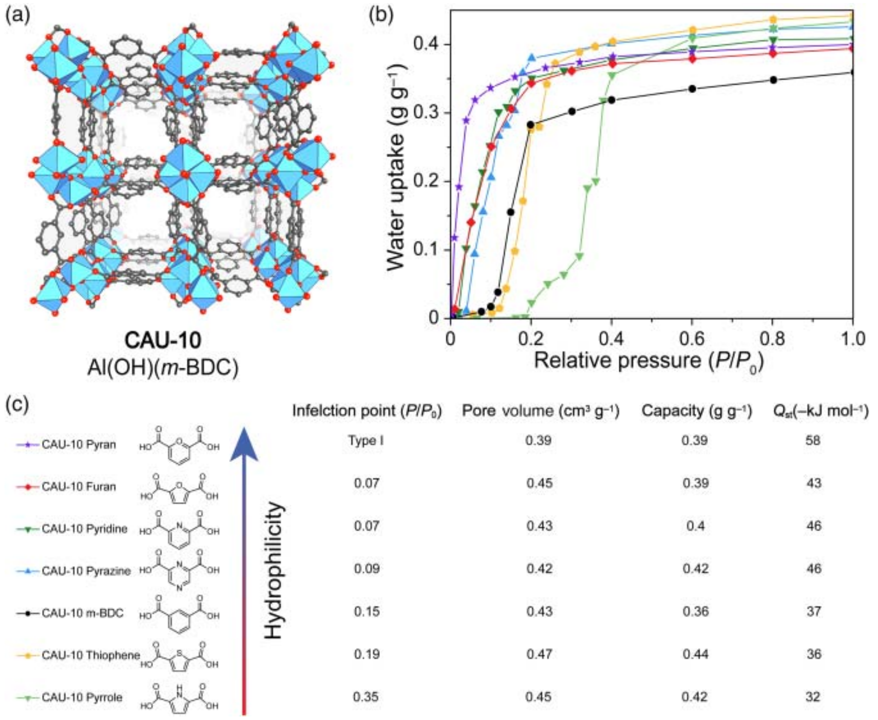

	Infelction point (P/P_0)	Pore volume ($cm^3\ g^{-1}$)	Capacity ($g\ g^{-1}$)	Q_{st}(−kJ mol^{-1})
★ CAU-10 Pyran	Type I	0.39	0.39	58
◆ CAU-10 Furan	0.07	0.45	0.39	43
▼ CAU-10 Pyridine	0.07	0.43	0.4	46
▲ CAU-10 Pyrazine	0.09	0.42	0.42	46
● CAU-10 m-BDC	0.15	0.43	0.36	37
● CAU-10 Thiophene	0.19	0.47	0.44	36
▼ CAU-10 Pyrrole	0.35	0.45	0.42	32

Figure 17.19 (a) Crystal structure of CAU-10 (**yfm**) with view along the *c*-direction. Source: Reinsch et al. 2012 [22]. Reproduced with permission of ACS.
(b) Water adsorption isotherms of CAU-10 analogs. All materials are isostructural and consequently the shift of the inflection point and the changes in the isosteric heat of adsorption are solely correlated to the hydrophilicity of the linker molecule.

17.8 Summary

In this chapter, we introduced the principles of water adsorption in MOFs. We first presented structural factors governing the thermodynamic and kinetic hydrolytic stability of MOFs and derived approaches to the design of hydrolytically stable MOFs therefrom. We discussed the possible water adsorption mechanisms and their correlation with the framework structure and specific structural features. We saw that the pore size has a strong effect on the shape of the isotherm and that large pores can even lead to irreversible water adsorption by capillary condensation. The effect of hydrophilic, hydroneutral, and hydrophobic functionalities on the shape of the water adsorption isotherm and the maximum capacity was discussed, revealing that hydrophilic groups shift the inflection point of the isotherm to lower relative pressures while hydrophobic groups shift it to higher relative pressure. This provides us with a tool to adjust the position of steep uptake by isoreticular functionalization. Subsequently, we discussed the two most studied applications with respect to water adsorption in MOFs: ADHPs and water harvesting from air. We illustrated the working principles of ADHPs and water harvesters, and conclude this chapter with considerations relevant to the design of next-generation materials for these applications.

References

1 (a) de Lange, M.F., Verouden, K.J., Vlugt, T.J. et al. (2015). Adsorption-driven heat pumps: the potential of metal-organic frameworks. *Chemical Reviews* 115 (22): 12205–12250. (b) Elsayed, E., Al-Dadah, R., Mahmoud, S. et al. (2017). CPO-27(Ni), aluminium fumarate and MIL-101(Cr) MOF materials for adsorption water desalination. *Desalination* 406: 25–36. (c) Ribeiro, A.M., Sauer, T.P., Grande, C.A. et al. (2008). Adsorption equilibrium and kinetics of water vapor on different adsorbents. *Industrial and Engineering Chemistry Research* 47 (18): 7019–7026. (d) Kanchanalai, P., Lively, R.P., Realff, M.J., and Kawajiri, Y. (2013). Cost and energy savings using an optimal design of reverse osmosis membrane pretreatment for dilute bioethanol purification. *Industrial and Engineering Chemistry Research* 52 (32): 11132–11141. (e) AbdulHalim, R.G., Bhatt, P.M., Belmabkhout, Y. et al. (2017). A fine-tuned metal-organic framework for autonomous indoor moisture control. *Journal of the American Chemical Society* 139 (31): 10715–10722. (f) Kim, H., Yang, S., Rao, S.R. et al. (2017). Water harvesting from air with metal-organic frameworks powered by natural sunlight. *Science* 356 (6336): 430–434.

2 Low, J.J., Benin, A.I., Jakubczak, P. et al. (2009). Virtual high throughput screening confirmed experimentally: porous coordination polymer hydration. *Journal of the American Chemical Society* 131 (43): 15834–15842.

3 DeCoste, J.B., Peterson, G.W., Jasuja, H. et al. (2013). Stability and degradation mechanisms of metal-organic frameworks containing the $Zr_6O_4(OH)_4$ secondary building unit. *Journal of Materials Chemistry A* 1 (18): 5642–5650.

4 (a) Choi, H.J., Dincă, M., Dailly, A., and Long, J.R. (2010). Hydrogen storage in water-stable metal-organic frameworks incorporating 1,3- and 1,4-benzenedipyrazolate. *Energy & Environmental Science* 3 (1): 117–123. (b) Colombo, V., Galli, S., Choi, H.J. et al. (2011). High thermal and chemical stability in pyrazolate-bridged metal-organic frameworks with exposed metal sites. *Chemical Science* 2 (7): 1311–1319.

5 Rieth, A.J., Yang, S., Wang, E.N., and Dincă, M. (2017). Record atmospheric fresh water capture and heat transfer with a material operating at the water uptake reversibility limit. *ACS Central Science* 3 (6): 668–672.

6 (a) Liu, J., Benin, A.I., Furtado, A.M. et al. (2011). Stability effects on CO_2 adsorption for the DOBDC series of metal-organic frameworks. *Langmuir* 27 (18): 11451–11456. (b) Kizzie, A.C., Wong-Foy, A.G., and Matzger, A.J. (2011). Effect of humidity on the performance of microporous coordination polymers as adsorbents for CO_2 capture. *Langmuir* 27 (10): 6368–6373.

7 (a) DeCoste, J.B., Peterson, G.W., Schindler, B.J. et al. (2013). The effect of water adsorption on the structure of the carboxylate containing metal-organic frameworks Cu-BTC, Mg-MOF-74, and UiO-66. *Journal of Materials Chemistry A* 1 (38): 11922–11932. (b) Jeremias, F., Lozan, V., Henninger, S.K., and Janiak, C. (2013). Programming MOFs for water sorption: amino-functionalized MIL-125 and UiO-66 for heat transformation and heat storage applications. *Dalton Transactions* 42 (45): 15967–15973.

8 (a) Guillerm, V., Ragon, F., Dan-Hardi, M. et al. (2012). A series of isoreticular, highly stable, porous zirconium oxide based metal-organic frameworks. *Angewandte Chemie International Edition* 51 (37): 9267–9271. (b) Bon, V., Senkovskyy, V., Senkovska, I., and Kaskel, S. (2012). Zr(IV) and Hf(IV) based metal-organic frameworks with reo-topology. *Chemical Communications* 48 (67): 8407–8409. (c) Bon, V., Senkovska, I., Baburin, I.A., and Kaskel, S. (2013). Zr-and Hf-based metal-organic frameworks: tracking down the polymorphism. *Crystal Growth and Design* 13 (3): 1231–1237. (d) Jiang, H.-L., Feng, D., Wang, K. et al. (2013). An exceptionally stable, porphyrinic Zr metal-organic framework exhibiting pH-dependent fluorescence. *Journal of the American Chemical Society* 135 (37): 13934–13938. (e) Furukawa, H., Gándara, F., Zhang, Y.-B. et al. (2014). Water adsorption in porous metal-organic frameworks and related materials. *Journal of the American Chemical Society* 136 (11): 4369–4381.

9 Dybtsev, D.N., Chun, H., and Kim, K. (2004). Rigid and flexible: a highly porous metal-organic framework with unusual guest-dependent dynamic behavior. *Angewandte Chemie International Edition* 116 (38): 5143–5146.

10 (a) Schoenecker, P.M., Carson, C.G., Jasuja, H. et al. (2012). Effect of water adsorption on retention of structure and surface area of metal-organic frameworks. *Industrial and Engineering Chemistry Research* 51 (18): 6513–6519. (b) Liang, Z., Marshall, M., and Chaffee, A.L. (2010). CO_2 adsorption, selectivity and water tolerance of pillared-layer metal organic frameworks. *Microporous and Mesoporous Materials* 132 (3): 305–310. (c) Tan, K., Nijem, N., Canepa, P. et al. (2012). Stability and hydrolyzation of metal organic frameworks with paddle-wheel SBUs upon hydration. *Chemistry of Materials* 24 (16): 3153–3167.

11 Bellarosa, L., Gutiérrez-Sevillano, J.J., Calero, S., and López, N. (2013). How ligands improve the hydrothermal stability and affect the adsorption in the IRMOF family. *Physical Chemistry Chemical Physics* 15 (40): 17696–17704.

12 Kang, I.J., Khan, N.A., Haque, E., and Jhung, S.H. (2011). Chemical and thermal stability of isotypic metal-organic frameworks: effect of metal ions. *Chemistry – A European Journal* 17 (23): 6437–6442.

13 (a) Cavka, J.H., Jakobsen, S., Olsbye, U. et al. (2008). A new zirconium inorganic building brick forming metal organic frameworks with exceptional stability. *Journal of the American Chemical Society* 130 (42): 13850–13851. (b) Valenzano, L., Civalleri, B., Chavan, S. et al. (2011). Disclosing the complex structure of UiO-66 metal organic framework: a synergic combination of experiment and theory. *Chemistry of Materials* 23 (7): 1700–1718.

(c) Wiersum, A.D., Soubeyrand-Lenoir, E., Yang, Q. et al. (2011). An evaluation of UiO-66 for gas-based applications. *Chemistry – An Asian Journal* 6 (12): 3270–3280.

14 Drisdell, W.S., Poloni, R., McDonald, T.M. et al. (2013). Probing adsorption interactions in metal-organic frameworks using X-ray spectroscopy. *Journal of the American Chemical Society* 135 (48): 18183–18190.

15 Dietzel, P.D., Johnsen, R.E., Blom, R., and Fjellvåg, H. (2008). Structural changes and coordinatively unsaturated metal atoms on dehydration of honeycomb analogous microporous metal-organic frameworks. *Chemistry – A European Journal* 14 (8): 2389–2397.

16 Do, D., Junpirom, S., and Do, H. (2009). A new adsorption–desorption model for water adsorption in activated carbon. *Carbon* 47 (6): 1466–1473.

17 Wißmann, G., Schaate, A., Lilienthal, S. et al. (2012). Modulated synthesis of Zr-fumarate MOF. *Microporous and Mesoporous Materials* 152: 64–70.

18 Akiyama, G., Matsuda, R., Sato, H. et al. (2012). Effect of functional groups in MIL-101 on water sorption behavior. *Microporous and Mesoporous Materials* 157: 89–93.

19 Jeremias, F., Khutia, A., Henninger, S.K., and Janiak, C. (2012). MIL-100(Al, Fe) as water adsorbents for heat transformation purposes – a promising application. *Journal of Materials Chemistry* 22 (20): 10148–10151.

20 Ko, N., Choi, P.G., Hong, J. et al. (2015). Tailoring the water adsorption properties of MIL-101 metal-organic frameworks by partial functionalization. *Journal of Materials Chemistry A* 3 (5): 2057–2064.

21 (a) Gutmann, V. (1976). Empirical parameters for donor and acceptor properties of solvents. *Electrochimica Acta* 21 (9): 661–670. (b) Gutmann, V. (1978). *Donor–Acceptor Approach to Molecular Interactions*. Plenum Press. (c) Sagawa, N. and Shikata, T. (2014). Are all polar molecules hydrophilic? Hydration numbers of nitro compounds and nitriles in aqueous solution. *Physical Chemistry Chemical Physics* 16 (26): 13262–13270.

22 Reinsch, H., van der Veen, M.A., Gil, B. et al. (2012). Structures, sorption characteristics, and nonlinear optical properties of a new series of highly stable aluminum MOFs. *Chemistry of Materials* 25 (1): 17–26.

23 Shigematsu, A., Yamada, T., and Kitagawa, H. (2011). Wide control of proton conductivity in porous coordination polymers. *Journal of the American Chemical Society* 133 (7): 2034–2036.

24 Chua, K., Chou, S., and Yang, W. (2010). Advances in heat pump systems: a review. *Applied Energy* 87 (12): 3611–3624.

25 (a) Metz, B., Solomon, S., Kuijpers, L. et al. (2005). *Safeguarding the Ozone Layer and the Global Climate System: Issues Related to Hydrofluorocarbons and Perfluorocarbons*. Cambridge University Press. (b) Velders, G.J., Andersen, S.O., Daniel, J.S. et al. (2007). The importance of the Montreal protocol in protecting climate. *Proceedings of the National Academy of Sciences* 104 (12): 4814–4819. (c) Oberthür, S. (2001). Linkages between the Montreal and Kyoto protocols – enhancing synergies between protecting the ozone layer and the global climate. *International Environmental Agreements: Politics, Law and Economics* 1 (3): 357–377.

26 Ehrenmann, J., Henninger, S.K., and Janiak, C. (2011). Water adsorption characteristics of MIL-101 for heat-transformation applications of MOFs. *European Journal of Inorganic Chemistry* 2011 (4): 471–474.

27 Küsgens, P., Rose, M., Senkovska, I. et al. (2009). Characterization of metal-organic frameworks by water adsorption. *Microporous and Mesoporous Materials* 120 (3): 325–330.

28 (a) Henninger, S.K., Jeremias, F., Kummer, H., and Janiak, C. (2012). MOFs for use in adsorption heat pump processes. *European Journal of Inorganic Chemistry* 2012 (16): 2625–2634. (b) Deria, P., Bury, W., Hod, I. et al. (2015). MOF functionalization via solvent-assisted ligand incorporation: phosphonates vs carboxylates. *Inorganic Chemistry* 54 (5): 2185–2192.

29 Vörösmarty, C.J., Green, P., Salisbury, J., and Lammers, R.B. (2000). Global water resources: vulnerability from climate change and population growth. *Science* 289 (5477): 284–288.

30 (a) Schemenauer, R.S. and Cereceda, P. (1994). A proposed standard fog collector for use in high-elevation regions. *Journal of Applied Meteorology* 33 (11): 1313–1322. (b) Klemm, O., Schemenauer, R.S., Lummerich, A. et al. (2012). Fog as a fresh-water resource: overview and perspectives. *Ambio* 41 (3): 221–234. (c) Park, K.-C., Chhatre, S.S., Srinivasan, S. et al. (2013). Optimal design of permeable fiber network structures for fog harvesting. *Langmuir* 29 (43): 13269–13277. (d) Wahlgren, R.V. (2001). Atmospheric water vapour processor designs for potable water production: a review. *Water Research* 35 (1): 1–22. (e) Muselli, M., Beysens, D., Marcillat, J. et al. (2002). Dew water collector for potable water in Ajaccio (Corsica Island, France). *Atmospheric Research* 64 (1): 297–312. (f) Clus, O., Ortega, P., Muselli, M. et al. (2008). Study of dew water collection in humid tropical islands. *Journal of Hydrology* 361 (1–2): 159–171. (g) Lee, A., Moon, M.-W., Lim, H. et al. (2012). Water harvest via dewing. *Langmuir* 28 (27): 10183–10191.

31 Fathieh, F., Kalmutzki, M.J., Kapustin, E.A. et al. (2018). Practical water production from desert air. *Science Advances* 4 (6): eaat3198.

32 Yang, S., Huang, X., Chen, G., and Wang, E.N. (2016). Three-dimensional graphene enhanced heat conduction of porous crystals. *Journal of Porous Materials* 23 (6): 1647–1652.

33 Canivet, J., Bonnefoy, J., Daniel, C. et al. (2014). Structure-property relationships of water adsorption in metal-organic frameworks. *New Journal of Chemistry* 38 (7): 3102–3111.

34 Cadiau, A., Lee, J.S., Damasceno Borges, D. et al. (2015). Design of hydrophilic metal organic framework water adsorbents for heat reallocation. *Advanced Materials* 27 (32): 4775–4780.

35 (a) Horcajada, P., Chalati, T., Serre, C. et al. (2010). Porous metal-organic-framework nanoscale carriers as a potential platform for drug delivery and imaging. *Nature Materials* 9 (2): 172–178. (b) Singh, R., Gautam, N., Mishra, A., and Gupta, R. (2011). Heavy metals and living systems: an overview. *Indian Journal of Pharmacology* 43 (3): 246. (c) Tchounwou, P.B., Yedjou, C.G., Patlolla, A.K., and Sutton, D.J. (2012). *Molecular, Clinical and Environmental Toxicology*, 133–164. Springer. (d) Venugopal, B. and Luckey, T.D. (1978). Metal toxicity in mammals. In: *Chemical Toxicity of Metals* *and Metalloids*, vol. 2. Plenum Press. (e) Domingo, J. (1994). Metal-induced developmental toxicity in mammals: a review. *Journal of Toxicology and Environmental Health, Part A Current Issues* 42 (2): 123–141.

36 (a) Fröhlich, D., Henninger, S.K., and Janiak, C. (2014). Multicycle water vapour stability of microporous breathing MOF aluminium isophthalate CAU-10-H. *Dalton Transactions* 43 (41): 15300–15304. (b) Borges, D.D., Maurin, G., and Galvão, D.S. (2017). Design of porous metal-organic frameworks for adsorption driven thermal batteries. *MRS Advances* 2 (9): 519–524.

37 Ghosh, P., Colón, Y.J., and Snurr, R.Q. (2014). Water adsorption in UiO-66: the importance of defects. *Chemical Communications* 50 (77): 11329–11331.